Spatio-temporal evolution of volcano seismicity: A laboratory study

Philip M Benson[1†*], Sergio Vinciguerra[2], Philip G Meredith[3], and R Paul Young[1]

[1] Lassonde Institute, University of Toronto, 170 College Street, Toronto, Ontario, M5S 3E3, CANADA.

[2] Istituto Nazionale di Geofisica e Vulcanologia, Sezione di Roma 1, Via di Vigna Murata 605, 00143, Rome, ITALY

[3] Rock and Ice Physics Laboratory, Department of Earth Sciences, University College London, Gower Street, London, WC1E 6BT, U.K.

*Corresponding author: p.benson@ucl.ac.uk

† Permanent address: Rock and Ice Physics Laboratory, Department of Earth Sciences, University College London, Gower Street, London, WC1E 6BT, U.K.

Abstract

We report a laboratory and microstructural study of a suite of deformation experiments in which basalt from mount Etna volcano is deformed and fractured at an effective confining pressure representative of conditions under a volcanic edifice (40 MPa). Particular attention was paid to the formation of a fracture and damage zone with which to stimulate coupled hydro-mechanical interactions that create the various types of seismicity recorded on volcanic edifices, and which usually precede eruption. Location of AE events through time shows the formation of a fault plane during which waveforms exhibit the typical high frequency characteristics of volcano-tectonic (VT) earthquakes. We found that these VT earthquakes were particularly pronounced when generated using dry samples, compared to samples saturated with a pore fluid (water). VT events generated during deformation of water saturated sample are characterised by a distinctive high frequency onset and a longer, low frequency coda exhibiting properties often seen in the field as hybrid events. We present evidence that hybrid events are, in fact, the common type of volcanic seismic event with either VT or low frequency (LF) events representing end members, and whose proportion depend on pore fluid being present in the rock type being deformed, as well as how close the rock is to failure. We find a notable trend of reducing instances of hybrid events leading up to the failure stage in our experiments, suggesting that during this stage, the pore fluid present in the rock moves sufficiently quickly to provide a resonance, seen as a LF coda. Our data supports recent modeling and field studies that postulate that hybrid events generated in volcanic areas are likely to be generated through the interaction of hydrothermal fluids moving through a combination of pre-existing microcrack networks and larger faults, such as those we observe in forensic (post-test) examination.

Keywords:

Volcanotectonics, Acoustic Emission, Rock Physics, Seismology, Hazard.

1. Introduction

The detection, measurement and analysis of seismicity in active volcanic areas is the key tool in volcanic hazard mitigation (e.g. Aki and Richards, 1980; McNutt, 1996; Chouet, 2003). Volcanic seismicity and monitoring technologies have been used with great success to forecast and analyze eruptive episodes in numerous settings, whether driven by explosive volcanism (Rowe et al., 1998; Kilburn and Voight, 1998) or more effusive processes (Patane et al., 2003). However, although our understanding of the spatio-temporal processes driving these observations has increased substantially with the wide scale adoption of new and improving technologies, such as modern broadband seismology and GPS, there is still no universally accepted quantitative physical model for determining whether or not a sequence of precursory phenomena will end in an eruption and for forecasting the time or the type of eruption. Part of the forecasting challenge is similar to that experienced with earthquakes; often, little data is observed before a catastrophic main eruption, requiring novel and innovative statistical strategies in order to arrive at a failure forecast (e.g. Kilburn, 2004). Central to these strategies is the application of fundamental rock mechanics in assessing the failure of the rock mass (analysed as the seismic event rate), whether driven by tectonic stresses of volcanically driven fluid pressures.

However, despite the plethora of data and models, most strategies for forecasting volcanic eruptive episodes rely on long-term observation and monitoring of the edifice, and numerical modeling (e.g. resonating cracks/faults and magma slug ascent), rather than directly assessing the fundamental micromechanics of the rock/fluid interactions. This is primarily due to the paucity of direct experimental evidence as these processes can only be observed, indirectly, at the volcanic vent. The picture is further complicated by the diverse ways that volcanic activity is ultimately manifested on the edifice, ranging from effusive and relatively benign volcanism to explosive plinian eruptions (Dingwell, 1996; McNutt, 2005). In order to understand some of these processes, more laboratory data is required, in particular the physical conditions responsible for, and which may enhance the rate and magnitude of, the three key types of volcano-tectonic seismicity. Firstly, Volcano Tectonic (VT) earthquakes, which are generated by deformation and faulting. Secondly, Low Frequency (LF) earthquakes, which are created by fluid flow though damage zones (e.g. Chouet, 1996; McNutt, 2005). This type of volcano seismicity in particular, measured from both field and laboratory, has greatly elucidated our knowledge of subsurface volcanic-tectonic processes (Burlini et al., 2007; Benson et al., 2008), even suggesting, for a time, a potential route to accurate forecasting methods (Chouet, 1996; Neuberg et al., 2006). Finally, the third type of seismicity shows features of both HF seismicity and also LF harmonic tremor. Known as hybrid events, this type of seismicity is characterised by a high frequency, VT-like onset and a low frequency LF-like coda, suggesting that hybrid generation is promoted by stress regimes leading to both rock failure, and also where fluids are present in order to generate LF and tremor (Chouet, 1996; White et al., 1998; Chouet, 2003).

In this paper, we address some of the these challenges by focusing on the generation and the interaction/switch between VT, LF and hybrid type events using laboratory rock physics in order to control and monitor the conditions of interest. Although the conditions of generation for VT and LF events is generally well understood, the method by which these types of seismicity switches and evolves into hybrid events, and vice versa, is poorly understood; and yet would reveal considerable information about the state of the magmatic plumbing system in terms of fluid pressures and ultimately contribute to improved forecast models (White et al., 1998). Whilst it is well known that gas, water/steam phase changes, dusty gasses and their associated interaction with the surrounding rock all play subtle roles in generating the LF events and tremor on the edifice (Kumagai et al., 2002), the generation of hybrid events has so far not been explored in detail in terms of its potential in failure forecasting.

2. Experimental rock physics as a laboratory tool

2.1 Sample description

The material tested is a porphyritic, alkali, lava-flow basalt from Etna volcano, Italy. It comprises millimetre-sized phenocrysts of pyroxene, olivine and feldspar in a fine-grained groundmass (Stanchits et al., 2006; Benson et al., 2007). The initial density of the block used in this study was 2860 kg/m^3 and the initial porosity was 3.8%, as measured via the standard ISRM triple weight water saturation method. Samples of 125 mm length and 50 mm diameter were prepared using a diamond coring drill, with the end faces ground flat and parallel to within 0.01 mm. In addition, a small conduit of 3.125mm diameter was pre-drilled down the centre axis of the sample in order to provide direct pore fluid access to the damage/fault zone formed during deformation and failure of the sample. This basalt was specifically chosen as previous studies have shown that it has a ubiquitous network of pre-existing microcracks. This microstructure is reflected in an anomalously low P-wave velocity of approximately 3250 m.s^{-1} (ambient conditions), and a relatively high permeability (steady-state-flow with water) in the range 1 to 4 x 10^{-17} m^2 at effective pressures from 5 to 50 MPa (Benson et al., 2006).

2.2 Experimental conditions and equipment

Deformation experiments were performed using a stiff, servo-controlled triaxial testing machine installed at the University of Toronto. The pressure vessel (Ergotech, Ltd.) is capable of achieving confining pressures ($\sigma_2 = \sigma_3$) of up to 100 MPa and a maximum principal axial stress (σ_1) of approximately 680 MPa across a 50 mm diameter sample (Fig. 1). For the experiments reported here, samples were deformed at a constant axial strain rate of 5 x 10^{-6} s^{-1}, controlled via linear variable displacement transducers (LVDTs). Two types of experiment were performed, an unsaturated experiment with an effective confining pressure of 40 MPa, and a saturated experiment using a constant pore fluid pressure (de-ionized/distilled water) of 20 MPa maintained by means of two servo-controlled pore pressure intensifiers, which are also fitted with an integral LVDTs that allows their use as volumometers. A rubber jacket separates the rock sample from the confining medium (silicone oil). A confining pressure of 60 MPa was used for these experiments in order to yield the same effective pressure of 40 MPa as for unsaturated tests; conditions broadly representative of those at approximately 1.5 km depth within a volcanic edifice.

Compressional (P) wave velocity measurements were made via an ultrasonic transducer embedded in the loading rams and in the rubber confining jacket (Fig. 1), with received voltages digitized and recorded on a digital storage oscilloscope at 50 MHz sampling frequency. Acoustic emissions (AEs) were recorded using 16 PZT crystals (of 1 MHz central frequency) embedded in the rubber jacket and also mounted within the steel loading platens (Fig. 1). The AE signal was split using buffered 60 dB preamplifiers (ASC, Ltd) between two recording systems: An ESG Hyperion AE recorder capable of storing 40 Gb of data on a circular Random Access Memory (equivalent to a moving window of the preceding 134 s of full-waveform experimental data in the configuration described here), and an ASC Richter AE system which records AE voltage data continuously to hard disk over a maximum of four hours for subsequent processing or 're-harvesting'. These are important attributes, since the rapid acceleration to failure often observed in the final phase of triaxial deformation of brittle rocks is commonly accompanied by a supra-exponential increase in AE activity (Meredith et al., 1990). This can cause conventional 'triggered' AE recorders to miss important events during the mask-time required to transfer data from volatile memory to permanent storage (Benson et al., 2007; Thompson et al., 2009).

2.3 Deformation and pore fluid decompression experiments

Standard triaxial deformation experiments were performed in which the sample is loaded at a constant strain rate until failure occurs (Fig. 2). At this stage the fault plane, which forms typically at an angle of approximately 30°, is connected to the pore fluid intensifiers via the conduit (hereafter called the sample failure stage). For water saturated experiments, an additional experimental step was carried out, in which the deviatoric stress is lowered until a hydrostat of 40 MPa effective pressure is achieved is order to ensure that no slip occurs on the fault plane. The pressurized pore fluid is then vented rapidly (< 0.2 s) via a simple needle valve (hereafter referred to as the decompression stage). The rapid release of the pore water pressure has the effect of stimulating rapid fluid movement through the fault and associated damage zone, through access provided via the central conduit and up though a top steel guide plate that connects to the vent valve (Fig. 1). In addition, some post-test field emission scanning electron micrographs (FESEM) were analyzed, based on the location of AE events, to confirm the deformation style and type (Benson et al., 2008). In this paper, we concentrate on the initial (deformation) stage of the experiment in order to elucidate the changing style of the signal, i.e. from hybrid/VT to LF, or otherwise.

3. Experimental results

Mechanical data for the two experiments is plotted in Figure 2. For the samples saturated with pore fluid (water), a noticeably lower peak stress is evident, of 520 MPa for sample EB2E1 compared to the dry sample (EB3E2) where failure occurred at a peak stress of 575 MPa. The reason behind this observation is straightforward, as water acts to reduce strength of the sample as cracks nucleate and propagate through the process of stress corrosion (Amitrano and Helmstetter, 2006). The rate of microcracking during loading is indicated by the AE hit rate, defined as bulk AE ‘hits’ averaged over the 16 AE sensors per second, with a ‘hit’ defined as every instance that a pre-set number of sensors (6) register voltage above a set threshold (60 mV). For water-saturated samples (fig), AE rate builds up slowly, reflecting the time dependent effect of water assisted sub-critical crack growth (Read et al., 1995). As maximum stress is approached the acoustic emission (AE) hit rate increases at an ever increasing rate, entering the well known supra-exponential phase (Benson et al., 2007) as the sample fails. For this particular sample, a second stress drop and accompanying peak in AE hit rate is also clearly seen. This is due to the specific fracture system formed, which has a main fault plane and a conjugate, both of which were independently seen in the AE record (Fig. 3). For dry sample deformation (Fig. 3B), a different trend in the AE hit record is seen, with AE build-up commencing at 2500s - 3000s and becoming noticeable at 4000s, far earlier that for the water saturated experiment, where a notable AE buildup occurs at approximately 5200s, only 90s (approximately) before peak stress. We interpret this effect as also being due to lack of pore fluid, without which the deformation is accommodated purely through rapid nucleation of microcracks rather than the stress corrosion process, which releases less energy. In both cases, the supra-exponential acceleration of AE occurs as sample failure approaches, at approximately 5200s for saturated samples (Fig. 3A) and approximately 5050s for non-saturated samples (Fig. 3B).

During the deformation stage of each sample, a triaxial velocity field is measured using an embedded triaxial (3-axis) P-wave transducer assembly. This assembly is dedicated to the measurement of the P-wave velocity (and its anisotropy) and is separate to the AE array so that interference is avoided and time spent listening to AE is maximized. In detail, the assembly uses three pairs of P-wave transducers in each of 'X', 'Y' and 'Z' (orthogonal) directions, with the 'Z' direction corresponding to the sample vertical axis and the X-Y plane describing the sample radial plane. The P-wave velocity is considerably higher in the axial direction than for the radial direction, with an anisotropy (at failure) of approximately 20% ($\Delta V/V_{mean}$) for water saturated samples (Fig. 3B) and an anisotropy of approximately 35% for dry samples (Fig. 3A). In addition, the bulk P-wave velocity is also higher for water saturated samples than for dry samples. This observation is easily explained by the formation of micro-cracks creating anisotropy due to the formation of fractures aligned parallel to the sample axis, but with crack normals distributed randomly within the radial plane of the sample, providing a distinct signature (e.g. Schubnel et al., 2006) and allowing the triaxial P-wave assembly to provide a full signature with only three orthogonal measurements. Accurate measurement of this velocity field is important in order to derive hypocenter locations from the AE data, which were calculated using the arrival time from at least 6 independent arrivals (channels) with a downhill simplex algorithm (detailed in Falls *et al.*, 1993), using the measured anisotropic velocity structure detailed above (e.g. Benson et al., 2007; Thompson et al., 2009). We estimate our AE locations have a theoretical average accuracy of approximately ±1mm, consistent with previous work (Lockner, 1991; Benson et al. 2008; Thompson et al., 2009). Although complicated, sample EB2E1 shows a distinct fracture plane and a conjugate (Fig. 4) which is well described by the AE locations. When dry samples are deformed (Fig. 5), AE locations once again map to the fault plane, and with a noticeably higher magnitude compared to water saturated rock, providing additional evidence that the energy of fracture is higher in these conditions due to the lack of stress corrosion. An FESEM analysis on areas of interest (i.e. areas where AE locations are seen to be tightly clustered on the fault plane) confirm that these areas have a complex damage structure, with features such as cracks, commuted and pulverized rock. These features can be seen for both water saturated (Fig. 4C) and dry (Fig. 5C) samples.

Waveforms recorded during deformation of the water saturated samples frequently exhibit hybrid-type waveforms, characterized by a HF onset and a LF component to the tail (Fig. 4B), compared to waveforms received during deformation of dry samples in which almost all of the received waveforms consist of high frequency events (Fig. 5). Hybrid events are therefore likely to be produced by the dual process of crack nucleation and deformation producing the high frequency onset, and, once these fluid pathways are created, fluid moving through the damage/crack network producing the LF resonance seen in the coda of the waveforms. In the field, hybrid events are detected in a wide range of environments, from shallow lava dome growth, where fracturing of the dome is almost certainly accompanied by rapid fluid and gas movement (Miller et al., 1998; White et al., 1998); and deeper sources where cyclical pressurization of the volcanic plumbing systems is likely to lead to a rock-fluid interface producing a trigger combined with conduit or crack resonance that is manifested as the observed LF coda (Neuberg et al., 2006; Chouet, 1996; 2003). In addition, recent studies by Tuffen et al. (2008) and Lavallée et al. (2008) have shown that shearing of magma also leads to a seismogenic response, consistent with a hybrid event in which both brittle and ductile processes may be represented.

A side by side comparison shows this frequency change clearly (Fig. 6). In Figure 6A, a typical HF event from a dry sample is shown (top) with a spectrogram illustrating its power spectrum (upper-middle panel) and a power time plot for three key frequencies (lower-middle panel). The spectrogram and normalized power plots show clearly that the power is essentially monochromatic along the waveform, with slightly higher power levels at high frequencies (650 kHz), compared to power spectra at low frequencies (100 kHz). For both frequencies, a rapid drop-off in power level is seen. For hybrid events, the high frequency impulsive onset (Fig. 6B, top panel) initially contains significant power at high frequencies, which die out rapidly after approximately 150 μs (50 μs after waveform onset). After this time, a significant LF power component continues to be present, as is also evident from the normalized power plot (Fig 6B, lower-middle panel). The low frequency component persists for the entire waveform, unlike the high frequency component, giving hybrid events their distinctive 'hockey stick' appearance. Finally, Fig. 6C shows an example waveform of a purely LF event from the same experiment which are induced by venting the water pore fluid via the top part of the apparatus (Benson et al., 2008). This protocol has the effect of isolating the HF generation mechanism (microcracking) showing a clear LF signal with significant power at low frequencies (50-100 kHz), exhibiting the well known LF/VLF resonance seen in the field (Chouet, 1996).

In order to investigate the evolution of energy along each waveform, throughout each experiment, we developed a simple routine using MatLab™ to qualitatively analyze each spectrogram and to investigate how the frequency content changed though time, and for each event in the record. As seen in Figure 6, considerable differences in frequency and power spectrum are evident when comparing VT to hybrid events, in particular the 'hockey stick' shape to the spectrogram. By automatically identifying this shape, our routine assesses how this relative pattern evolves through the experiment with respect to the sample deformation and pore fluid under study.

The method proceeds in the following manner. Using the spectrograms as input, FFT's are analyzed covering the first 100 μs after initial onset (the initial onset occurs at 25% of trace length, at 100 μs, defined by the triggering criterion in the AE recorder). Energy is determined for each FFT 'slice' by taking the area under the power-time plot, and calculating log (energy) vs. FFT slice time along each waveform. This procedure is then averaged across all active, unclipped (unsaturated), channels in each event, resulting in a representation of how power changes over time, per event (Fig 6, lower panels). Typically, a break of slope is seen for hybrid events (Fig. 6B, lower panel), as the high energy HF impulsive onset dies out and switches to the LF resonance, which occurs fairly consistently at approximately 150 μs into each waveform (50 μs into the analysis window, or 50%). For VT events, no break of slope is generally seen, and the power change over FFT time slice is fairly high (slopes of ~0.04). For LF events there is likewise no change in slope. However, the slopes of the power change are smaller (~0.004), reflecting how the power in the LF tail decreases more gradually that for the VT types events. Although qualitative, this method is useful in our experiments by essentially identifying – in a self-consistent manner – the 'hockey stick' -like shape to the hybrid spectrogram. By plotting the slope of the line before and after this break, a simple determination can be made as to whether an event could be classed as VT or hybrid as each experiment proceeds, leading up to and including sample failure, and for each experiment type (water saturated or dry). By applying the same routine consistently to each experiment, we can therefore assess the change in hybrid content as the experiment progresses.

Figure 7 shows the results of this procedure applied to the dry experiment. During the approach to sample failure (event number 8000), an approximately linear increase in energy change per event (ΔEe) is calculated. Furthermore, the same trend is seen in both the first 50 μs and second 50 μs after first break, with the slope of each ΔEe window within calculation error. Not only does this provide evidence that the energy change per event is slowly decreasing (i.e. the negative slope seen in Fig. 6A becomes less steep), but that the change in the energy spread through the first 100 μs of the waveform is not changing. This type of response is typical of either a continuous LF tremor, or of a quasi-continuous fracturing process, in which the energy release is continuous over extended periods of time after initial onset. Inspection of the waveforms (Fig. 7) reveals the latter HF fracturing, as expected from experimental conditions, and with no discernable changing in frequency content during each event, i.e. hybrid events are not seen during fracturing of ‘dry’ Etna basalt.

Initially, for water saturated samples (Fig. 8), a higher value of ΔEe is calculated for the first 50μs after waveform impulse onset than for the second 50μs. However, as the sample deforms, the ΔEe values start to converge, starting from approximately event number 1100. Visual inspection of the spectrograms confirm that, initially, the events show the classic ‘hockey stick’ shape indicative of hybrid events, with a high frequency power component initially giving way to a lower frequency coda. As failure is approached (~ event 1400), the ΔEe slope of the first 50μs increases, resulting in the break of slope becoming less clear. Finally, as sample failure occurs – signified by the stress drop at event 1400 – the ΔEe plots converge to the same value (zero slope) within calculation error, indicating that the energy no longer changes with time over the period investigated. Although subtle, visual inspection of the spectrograms confirms this general trend, with the ‘hockey stick’ feature fading out through time and being gradually replaced by a spectrum with a strong LF component.

4. Discussion and conclusions

Due to the combination of pore fluid, high stresses and a dynamically fracturing system, it is likely that stress corrosion is a dominant mechanism in promoting new crack and fault growth, especially as this process allows new cracks to nucleate and coalesce at a lower stress as compared to when pore fluid is not present (Fig. 2). In addition, the addition of an active pore fluid allows fault growth to proceed with less emitted seismicity (Fig. 3). During the fracturing process, we observed a majority of hybrid events, likely to be caused by a combination of processes that (a) open new cracks and pathways and (b) the movement of the high pressure pore fluid which produces the LF coda (Fig. 4, 6). Post test FESEM analysis confirms this hypothesis, since we observe a significant and diverse microcrack and fracture array containing many constrictions and pinch-points that are likely to produce LF type events (Benson et al., 2008). Furthermore, we also observe the presence of finely comminuted rock particles in the cracks that have been in suspension in the pore fluid. Such suspended particles change the effective density of the pore fluid and hence its physical and transport properties. This is significant because the presence of ash and comminuted rock within natural volcanic fractures has been directly observed in the field as tuffisite veins (Tuffen and Dingwell, 2005), and has also been suggested to influence seismicity generation mechanisms (e.g., Kumagai, 2001) in terms of its effect upon the fluid density. Therefore, although not the primary focus of this work, our post-test observations are entirely consistent with these suggestions and provide some experimental evidence that future work on colloidal and multi-phase fluids may be important to further understanding of hybrid and LF generation mechanisms during shear fracture. In addition, seismicity generated during shearing of magmas has been postulated to be a source of hybrid events; also consistent with our laboratory observations (Tuffen et al., 2008; Lavallée et al., 2008). In this way, shearing and fracturing of fluid saturated systems – whether water or magma – can produce a diverse range of seismicity depending on the fluid content, suggesting that hybrid events may be the general form of volcano seismicity, with LF and VT events providing two end members that represent excessively slow or fast processes respectively (Fig. 6).

To further analyze the spread of hybrid events through the sample failure process, we investigated how the energy contained in the first and second 50 μs after the impulsive onset varied with time (event sequence number). These data show that as failure is approached in water saturated systems, the energy change contained in these two parameters starts to converge (Fig. 8). For unsaturated systems, this convergence is absent. Taken together, the combination of pore fluids and a dynamically fracturing system can create conditions needed for stimulating hybrid events that become LF events when the fluid conduits are sufficiently connected. This hypothesis has been tested by direct comparison to samples in which no fluid was present, exhibiting HF fracturing events only (Fig. 7). Although we note that the calibration of the type of AE sensors used in these – and other – studies remains a challenge, the sensor output response has been measured, which is approximately flat between ~15kHz and ~750kHz, allowing the type of relative measurements presented here to be made with confidence. A full calibration of AE sensors in terms of V/ms^{-1} is currently under investigation to permit comparison to surface seismic data, ultimately in order to attempt to elucidate the hybrid signals routinely measured on active volcanoes in terms of edifice deformation and hence an improved hazard mitigation strategy.

We conclude that stress corrosion has an important contribution to the micromechanics that occur on volcanic edifices due to the dynamic forces, pore pressures and temperatures inherent in these systems. Hybrid events are likely to be a general seismic signal which are generated in fluid saturated rock, with fracturing or conduit shearing (Neuberg et al., 2006; Tuffen et al., 2008) providing an initial impulse to the waveform. As crack networks and conduits are opened by the brittle processes, rapid fluid movement into the resulting voids provides a source of resonance through structures ranging from tortuous and undulating 'pinch-outs' to larger fractures and conduits where LF events are likely to be generated, depending on the individual system. LF events are likely to represent one end member of this general case, specifically to fluid movement without brittle fracturing or fault creep, with VT events providing another end member where pore fluids are not present or cannot move freely. Finally we provide laboratory evidence that a switch occurs from dominantly hybrid to dominantly LF type seismic events as failure is approached due to the fracture front creating a network of faults within which fluids are able to move and thus to generate signals recorded as LF events, implying that brittle processes remain key to assessing the stability of volcanoes from surface seismic data.

Acknowledgements

This work was partially supported by a Marie-Curie International Fellowship within the 6th European Community Framework program (contract MOIF-CT-2005-020167 to P.M.B.), project FIRB-MIUR (Sviluppo Nuove Tecnologie per la Protezione e Difesa del Territorio dai Rischi Naturali) to S.V.; and a CFI (Canadian Foundation for Innovation) award to R.P.Y. The authors gratefully thank Laszlo Lombos and Dylan Roberts at Ergotech Ltd. for assistance with instrument development and technical support, as well as Will Pettitt at Applied Seismology Consultants Ltd. for software development and advice. P.M.B. thanks Wai-lai Ying and Farzine Nasseri for experimental assistance. The authors further thank the editor and an anonymous reviewer whose comments greatly improved the manuscript.

References

Aki, K., and Richards, P.G. (1980), Quantitative seismology: Theory and methods, Freeman & Co., San Francisco.

Amitrano, D., and A. Helmstetter (2006), Brittle creep, damage, and time to failure in rocks, J. Geophys. Res., 111, B11201, doi:10.1029/2005JB004252.

Benson, P., A. Schubnel, S. Vinciguerra, C. Trovato, P. Meredith, and R. P. Young (2006), Modeling the permeability evolution of micro-cracked rocks from elastic wave velocity inversion at elevated isostatic pressure, J. Geophys. Res., 111, B04202, doi:10.1029/2005JB003710.

Benson, P. M., Thompson, B.D., Meredith, P.G., Vinciguerra, S., Young, R.P. (2007) Imaging slow failure in triaxially deformed Etna basalt using 3D acoustic-emission location and X-ray computed tomography. Geophys. Res. Lett., 34, L03303, 10.1029/2006GL028721.

Benson P.M., S. Vinciguerra, P.G. Meredith, and R.P. Young (2008), Laboratory Simulation of Volcano Seismicity, Science, 322, 249, doi: 10.1126/science.1161927.

Burlini, L., S. Vinciguerra, G. Di Toro, G. De Natale, P.G. Meredith, and J.-P. Burg (2007), Seismicity preceding volcanic eruptions: new experimental insights, Geology, 35, 183-186.

Chouet, B.A. (1996), Long-period volcano seismicity: its source and use in eruption forecasting, Nature, 380 , 309-316.

Chouet, B. (2003), Volcano seismology, Pure and Applied Geophysics, 160, 739-788.

Dingwell, D.B. (1996), Volcanic dilemma: flow or blow? Science 273 (5278), 1054–1055.

Falls, S.D. (1993), Ultrasonic Imaging and Acoustic Emission Studies of Microcrack Development in Lac Du Bonnet Granite, Ph.D. thesis, Department of Geological Sciences, Queen's University, Kingston, Ontario, Canada.

Foulger, G.R., B.R. Julian, D.P. Hill, A.M. Pitt, P.E. Malin, E. Shalev (2004), Non-double-couple microearthquakes at long valley caldera, California, provide evidence for hydraulic fracturing, J. Volc. Geotherm. Res., 132, 45-71.

Kilburn, C.R.J. and Voight, B. (1998), Slow rock fracture as eruption precursor at Soufriere Hills volcano, Montserrat, Geophys. Res. Lett., 25(19), 3665-3668.

Kilburn, C.R.J. (2004), Fracturing as a quantitative indicator of lava flow dynamics. J. Volcanol. Geotherm. Res. 132, 209–224.

Kumagai, H. and Chouet, B.A. (2001), The dependence of acoustic properties of a crack on the resonance mode and geometry, Geophys. Res. Lett., 28(17), 3325-3328.

Kumagai, H., Chouet, B.A., and Nakano, M. (2002), Waveform inversion of oscillatory signatures in long-period events beneath volcanoes: J. Geophys. Res., v. 107, n. B11, 2301, doi: 10.1029/2001JB001704.

Lockner, D. A., J. D. Byerlee, V. Kuksenko, A. Ponomarev, and A. Sidorin (1991), Quasi-static fault growth and shear fracture energy in granite, Nature, 350, 39–42.

Lavallée, Y., Meredith, P.G., Dingwell, D.B., Hess, K.-U., Wassermann, J., Cordonnier, B., Gerik, A., Kruhl, J.H. (2008), Seismogenic lavas and explosive eruption forecasting. Nature 453, 507–510.

McNutt, S.R. (1996), Seismic monitoring and eruption forecasting of volcanoes; a review of the state-of-the-art and case histories, in Monitoring and mitigation of volcanic of volcanoes, edited by R. Scarpa and R. Tilling, Springer & Verlag, New York.

McNutt, S.R. (2005), Volcanic seismology. Ann. Rev. Earth Planet. Sci. 33, 461–491.

Meredith, P.G., I. G. Main, and C. Jones (1990), Temporal variations in seismicity during quasi-static and dynamic rock failure, Tectonophysics, 175, 249 – 268.

Miller, A.D., R.C. Stewart, R.A. White, R. Luckerr, B.J. Baptie, W.P. Aspinall, J.L. Latchman, L.L. Lynch, and B. Voight (1998), Seismicity associated with dome growth and collapse at the Soufriere Hills Volcano, Montserrat, Geophys. Res. Lett., 25(18), 3401-3404.

Neuberg, J.W. (2000), Characteristics and causes of shallow seismicity in andesite volcanoes. Philos. Trans. R. Soc. London Ser. A 358, 1533-1546

Neuberg, J.W., H. Tuffen, L. Collier, D. Green, D. Dingwell (2006), The trigger mechanism of low-frequency earthquakes on Montserrat, J. Volc. Geotherm. Res., 153, 37–50.

Patane, D., P. De Gori, C. Chiarabba, A. Bonaccorso (2003), Magma ascent and the pressurisation of mount Etna's volcanic system, Science, 299, 2061-203

Read, M.D., M.R. Ayling, P.G. Meredith, and S.A.F. Murrell (1995), Microcracking during triaxial deformation of porous rocks monitored by changes in rock physical properties, II. Pore volumometry and acoustic emission measurements on water-saturated rocks, Tectonophysics, 245, 223-235.

Rowe, C.A., R.C. Aster, P.R. Kyle, T.W. Schule, and R.R. Dibble (1998), Broadband recording of Srombolian explosions and associated very-long-period seismic signals on Mount Erebus volcano, Ross Island, Antarctica, Geophys. Res. Lett., 25(13), 2297-2300.

Smith, R., et al. (2009), Fracturing of volcanic systems: Experimental insights into pre-eruptive conditions, Earth Planet. Sci. Lett., doi:10.1016/j.epsl.2009.01.032

Schubnel, A., P.M. Benson, B.D. Thompson, J.F. Hazard and R.P. Young (2006), Quantifying Damage, Saturation and Anisotropy in Cracked Rocks by Inverting Elastic Wave Velocities, Pure Appl. Geophys., 163, 947 – 973.

Stanchits, S., S. Vinciguerra, and G. Dresen (2006), Ultrasonic velocities, acoustic emission characteristics and crack damage of basalt and granite, Pure Appl. Geophys., 163, 974 – 993.

Thompson, B. D., R. P. Young, and D. A. Lockner (2009), Premonitory acoustic emissions and stick-slip in natural and smooth-faulted Westerly granite, J. Geophys. Res., 114, B02205, doi:10.1029/2008JB005753.

Tuffen, H. and Dingwell, D.B. (2005), Fault textures in volcanic conduits: evidence for seismic trigger mechanisms during silicic eruptions. Bull. Volcanol. 67 (4), 370–387.

Tuffen, H., Smith, R., Sammonds, P.R. (2008), Evidence for seismogenic fracture of silicic magma, Nature 453, 511-514.

White, R.A., Miller, A.D., Lynch, L., and Power, J. (1998), Observations of hybrid seismic events at Soufriere Hills Volcano, Montserrat: July 1995 to September 1996, Geophys. Res. Lett., 25(19), 3657-3660.

FIGURE CAPTIONS

Fig. 1. Detail of a typical experimental setup. Sample dimensions are 50 mm diameter by 125 mm length. For the water saturated experiment, a confining pressure of 60 MPa was used with a pore pressure of 20 MPa. For dry experiments, a confining pressure of 40 MPa was used. An array of 18 piezoelectric sensors to detect Acoustic Emission (AE) was arrayed around the sample (12) and embedded in the upper and lower steel platens (3 per platen), of which 16 were used for AE recording. In order to determine an accurate velocity model for source location inversion, a triaxial array of P-wave transducers was employed. A rubber jacket isolates the sample from the silicone oil confining medium.

Fig. 2. Plot of stress-strain for dry and water saturated samples. Peak stress for the unsaturated sample is noticeably higher than for samples saturated with pore fluid.

Fig. 3. Time-Stress (left axis), Time-AE hit rate (left axis) and Time-P-wave velocity (right axis) for Water saturated (A) and Unsaturated (B) samples. Equivalent strain is plotted on the upper axis. A triaxial velocity model, measured axially and radially during the loading ramp, is necessary for accurate calculation of AE hypocentres. For the water saturated sample, a noticeably higher velocity structure was measured compared to unsaturated samples, and also a lower AE hit rate. A P-wave anisotropy of 20% and 35% was measured at failure for saturated and unsaturated samples respectively, and was taken into account for AE location using horizontally anisotropic downhill simplex algorithm.

Fig. 4. Photograph of the water saturated sample taken post-test (panel A), with AE locations superimposed, and an FESEM montage taken normal (across strike) to the fault plane. Although this fracture exhibits a somewhat complicated, conjugate fault set, the AE maps well to the observed fracture. Panel B shows a selection of representative waveforms, showing a distinctive high frequency onset and low frequency component in the coda. FESEM micrographs of selected areas of AE (labelled) illustrates the highly fractured nature of the damage areas, and also numerous ‘pinch-outs’ and bottlenecks through which pore fluid flow is likely to generate the LF coda.

Fig. 5. Photograph of sample EB3-2 (unsaturated), post test (panel A), with AE locations superimposed. Once again, the AE maps well to the observed fault. Panel B shows a selection of representative waveforms, which are dramatically different in character to those seen in water saturated experiments (Fig. 4B); this time the waveforms consist entirely of a sharp, high frequency onset with no obvious low frequency resonance. Panel C again illustrates representative fracture and damage zones, with notable quantities of pulverized and commutated rock.

Fig. 6. Comparison between high frequency VT events (panel A), hybrid events (panel B), and LF events (panel C). The top row in each panel illustrates representative waveforms, with power spectrograms plotted underneath (colour denotes power). The middle row illustrates how power changes with time though each waveforms, at three selected frequencies, 600 kHz, 350 kHz, and 100 kHz. Hybrid events are characterised by a high frequency, impulsive onset, with lower frequency components in the coda; whereas VT events have little power at low frequencies and LF events have virtually no power at high frequencies. The bottom row of figures illustrates the changing slope of energy/time in the 100 μs after the first break, and how this can be used to qualitatively identify hybrid events from LF or VT (see text for detail).

Fig. 7. Analysis of the hybrid events using the energy change with time in the frequency-time plot for the first and second 50 μs after the initial impulsive onset measured sequentially across all located events shown in figure 6. Full detail of the method is explained in the text. For unsaturated samples the negligible difference in energy change over this interval (within the error of the method) is interpreted as representative of LF or HF events (i.e. Hybrids are not present, and the distinctive 'hockey stick' shape to the spectrogram is not seen). Typical error bars are shown for the first data point only.

Fig. 8. Analysis of the hybrid events using the energy change with time in the frequency-time plot for the first and second 50 μs after the initial impulsive onset measured sequentially across all located events shown in figure 4. Full details of the method is explained in the text. For water saturated samples, a distinct convergence is seen between the energy change contained in the first and second 50 μs of the waveform as the sample approaches failure. Typical error bars are shown for the first data point only.

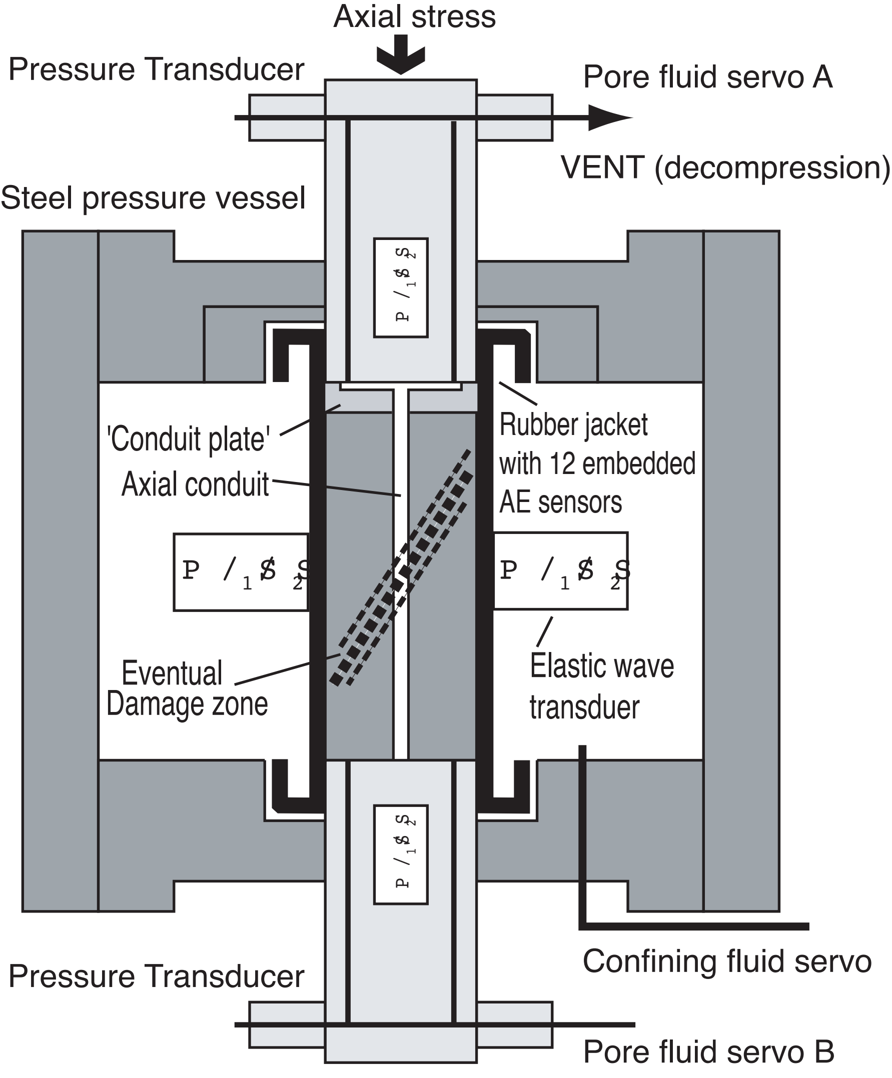

Axial stress
Pressure Transducer
Pore fluid servo A
VENT (decompression)
Steel pressure vessel
'Conduit plate'
Axial conduit
Rubber jacket
with 12 embedded
AE sensors
Eventual
Damage zone
Elastic wave
transduer
Confining fluid servo
Pressure Transducer
Pore fluid servo B

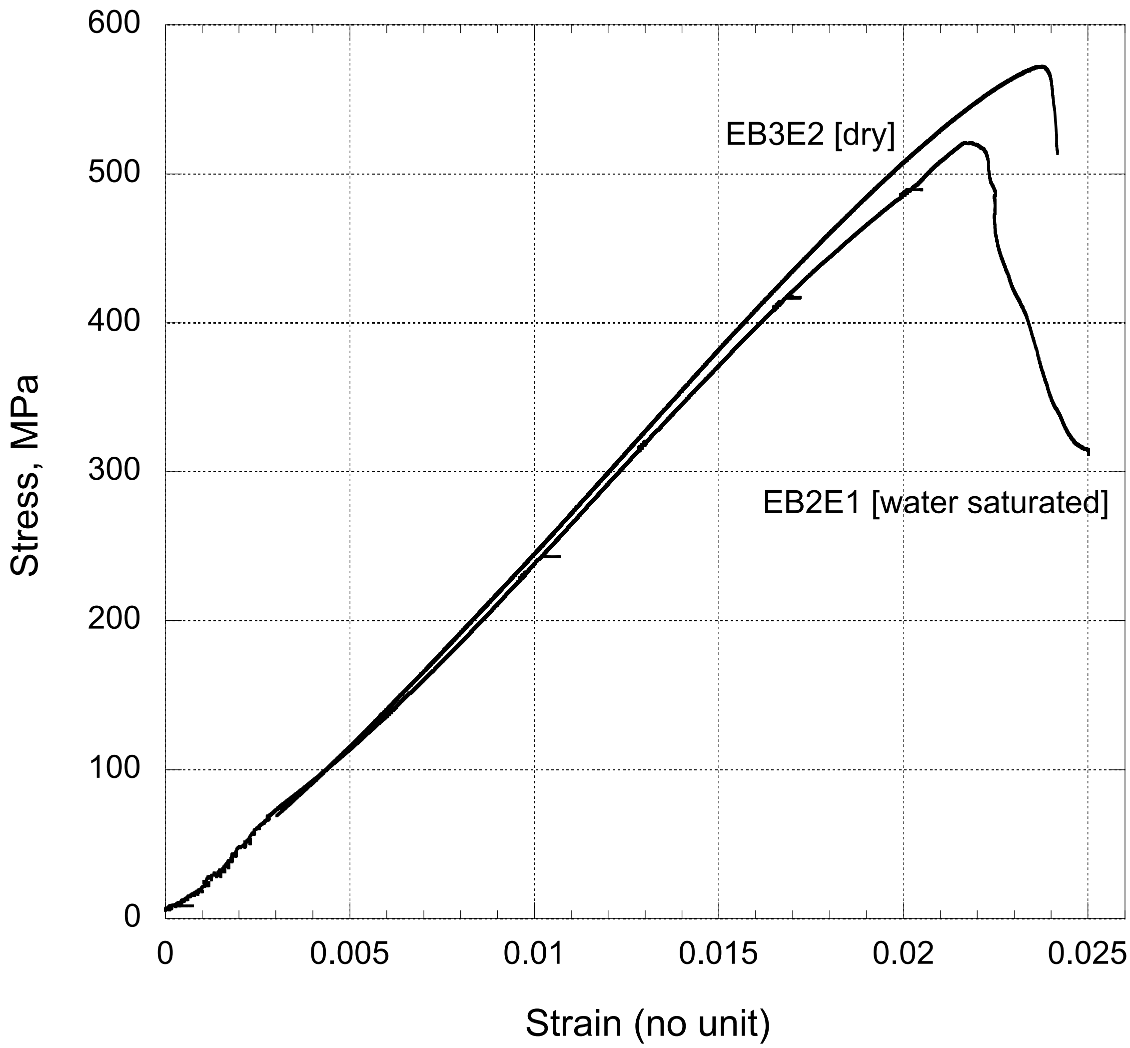

600
500
400
300
200
100
0
Stress, MPa
0
0.005
0.01
0.015
0.02
0.025
Strain (no unit)
EB3E2 [dry]
EB2E1 [water saturated]

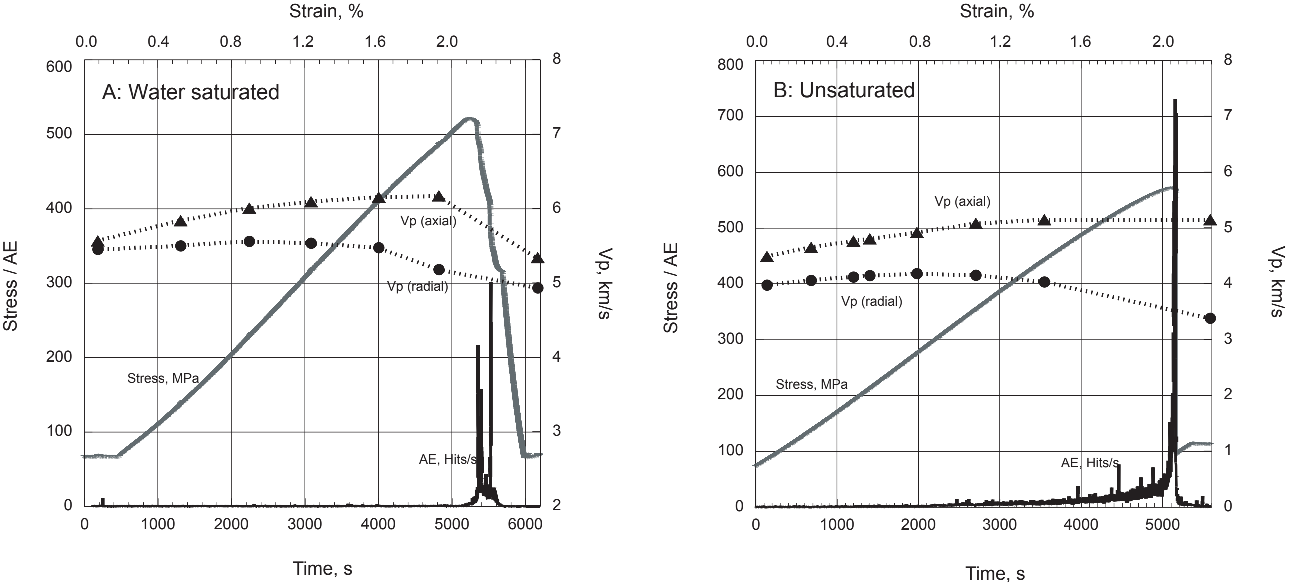

Strain, %
0.0
0.4
0.8
1.2
1.6
2.0
600
500
400
300
200
100
0
8
7
6
5
4
3
2
A: Water saturated
Vp (axial)
Vp (radial)
Stress, MPa
AE, Hits/s
Stress / AE
Vp, km/s
0
1000
2000
3000
4000
5000
6000
Time, s
Strain, %
0.0
0.4
0.8
1.2
1.6
2.0
800
700
600
500
400
300
200
100
0
8
7
6
5
4
3
2
1
0
B: Unsaturated
Vp (axial)
Vp (radial)
Stress, MPa
AE, Hits/s
Stress / AE
Vp, km/s
0
1000
2000
3000
4000
5000
Time, s

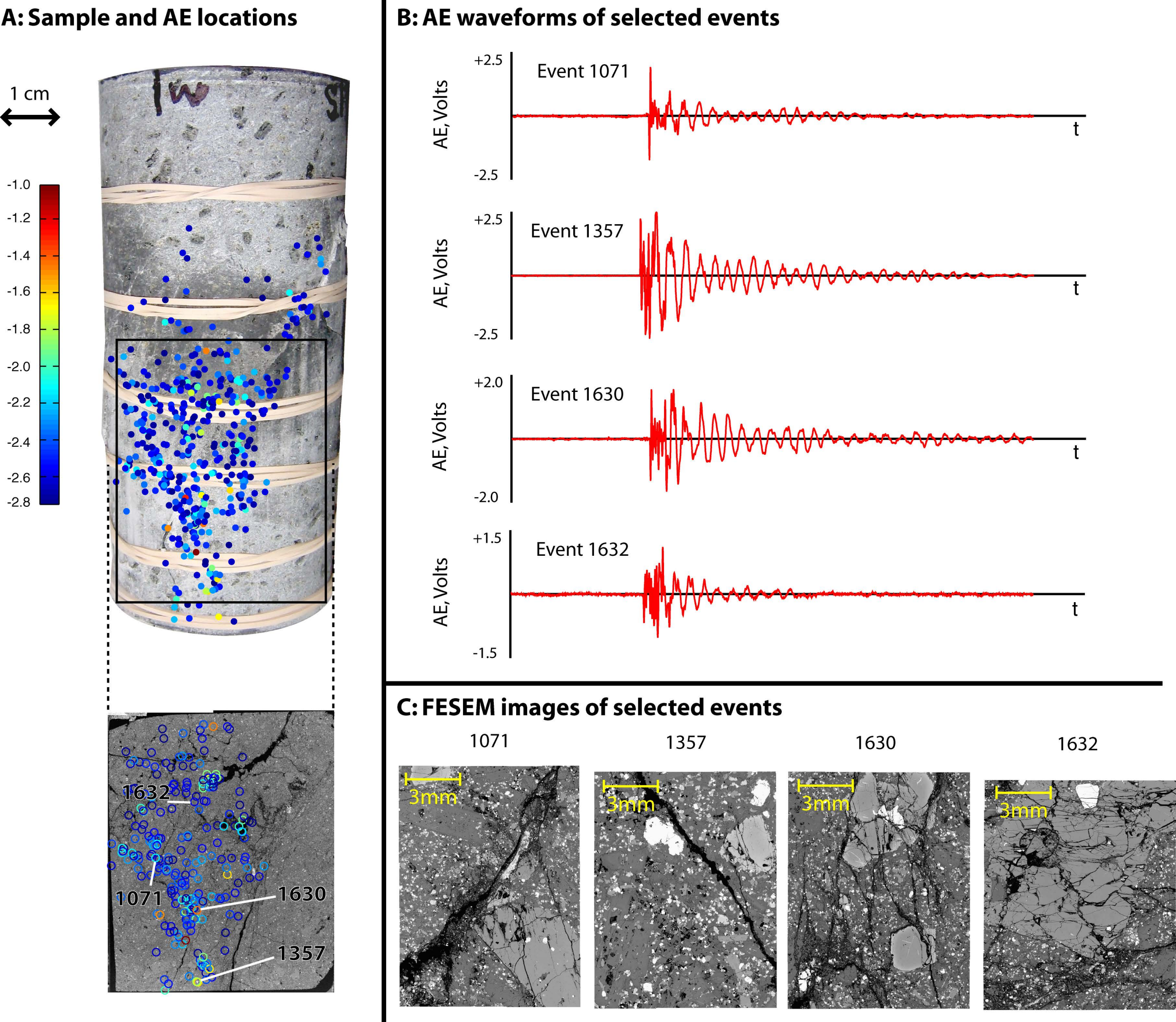

A: Sample and AE locations
1 cm
-1.0
-1.2
-1.4
-1.6
-1.8
-2.0
-2.2
-2.4
-2.6
-2.8
1632
1071
1630
1357
B: AE waveforms of selected events
+2.5
Event 1071
AE, Volts
-2.5
t
+2.5
Event 1357
AE, Volts
-2.5
t
+2.0
Event 1630
AE, Volts
-2.0
t
+1.5
Event 1632
AE, Volts
-1.5
t
C: FESEM images of selected events
1071
1357
1630
1632
3mm
3mm
3mm
3mm

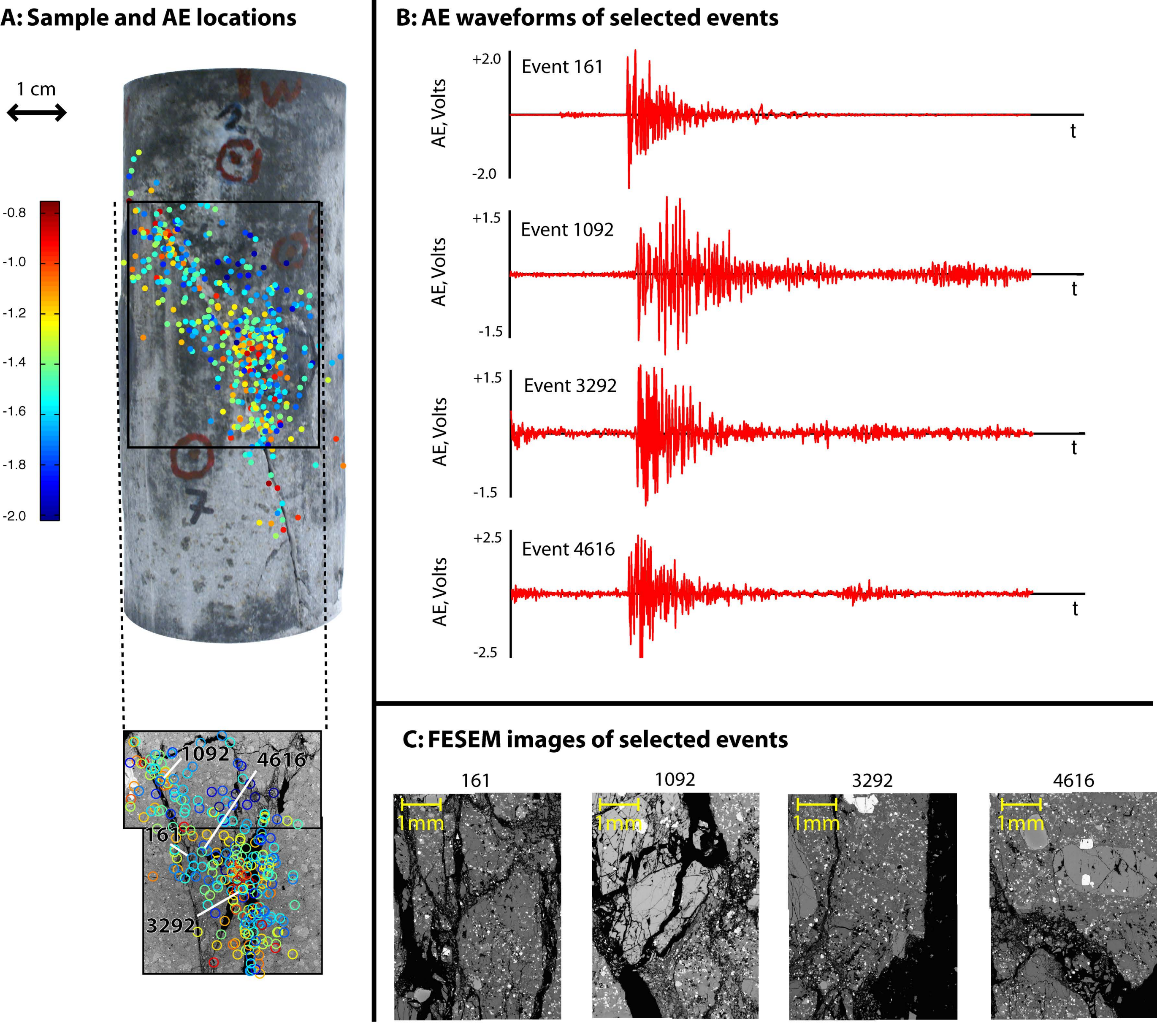
A: Sample and AE locations
1 cm
-0.8
-1.0
-1.2
-1.4
-1.6
-1.8
-2.0
1092
4616
161
3292
B: AE waveforms of selected events
+2.0
Event 161
AE, Volts
-2.0
t
+1.5
Event 1092
AE, Volts
-1.5
t
+1.5
Event 3292
AE, Volts
-1.5
t
+2.5
Event 4616
AE, Volts
-2.5
t
C: FESEM images of selected events
161
1092
3292
4616
1mm
1mm
1mm
1mm

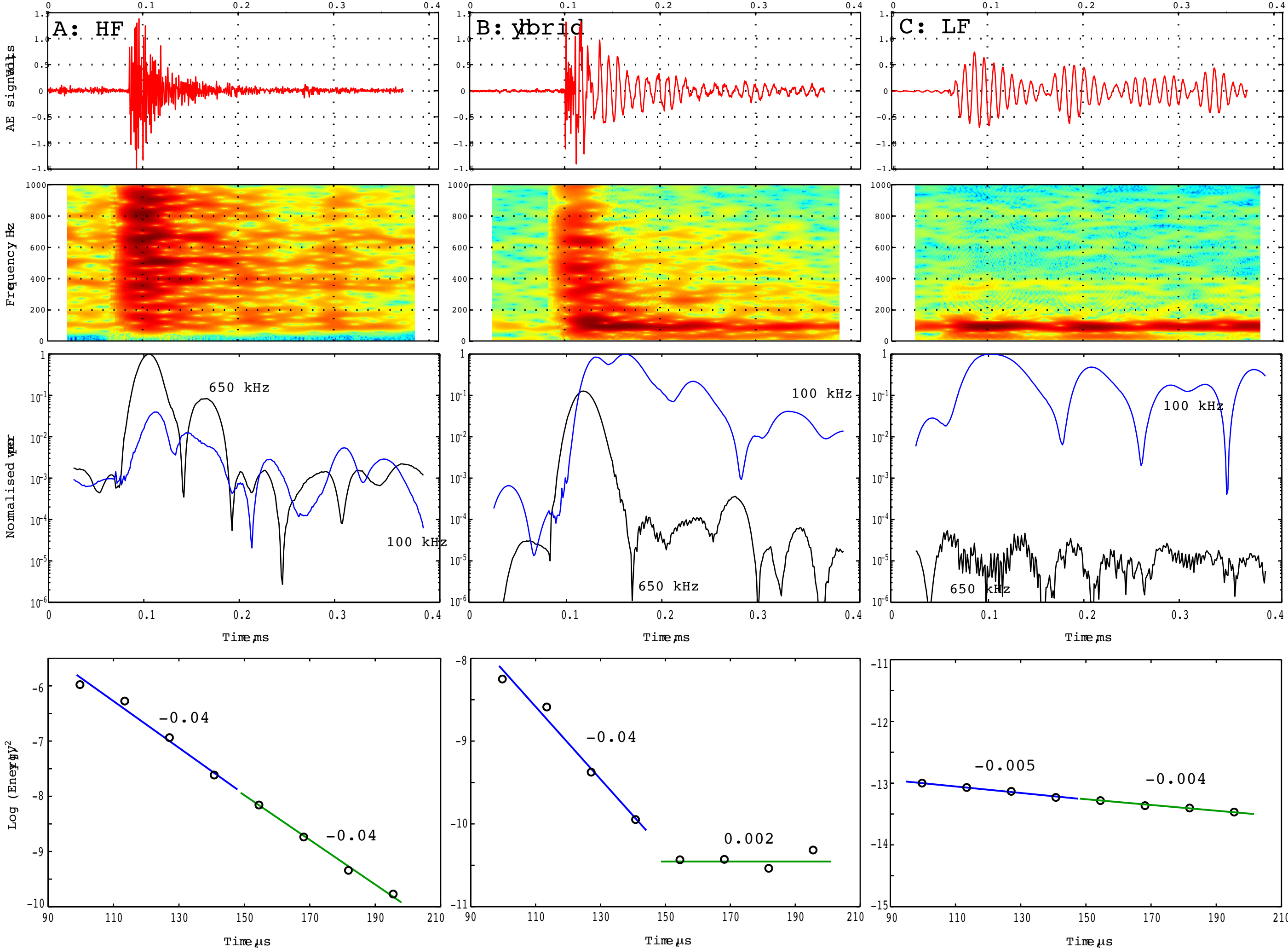
A: HF
B: Hybrid
C: LF
AE signal, Volts
Frequency, kHz
650 kHz
100 kHz
100 kHz
650 kHz
100 kHz
650 kHz
Normalised power
Time, ms
Time, ms
Time, ms
Log (Energy, V²)
-0.04
-0.04
-0.04
0.002
-0.005
-0.004
Time, µs
Time, µs
Time, µs

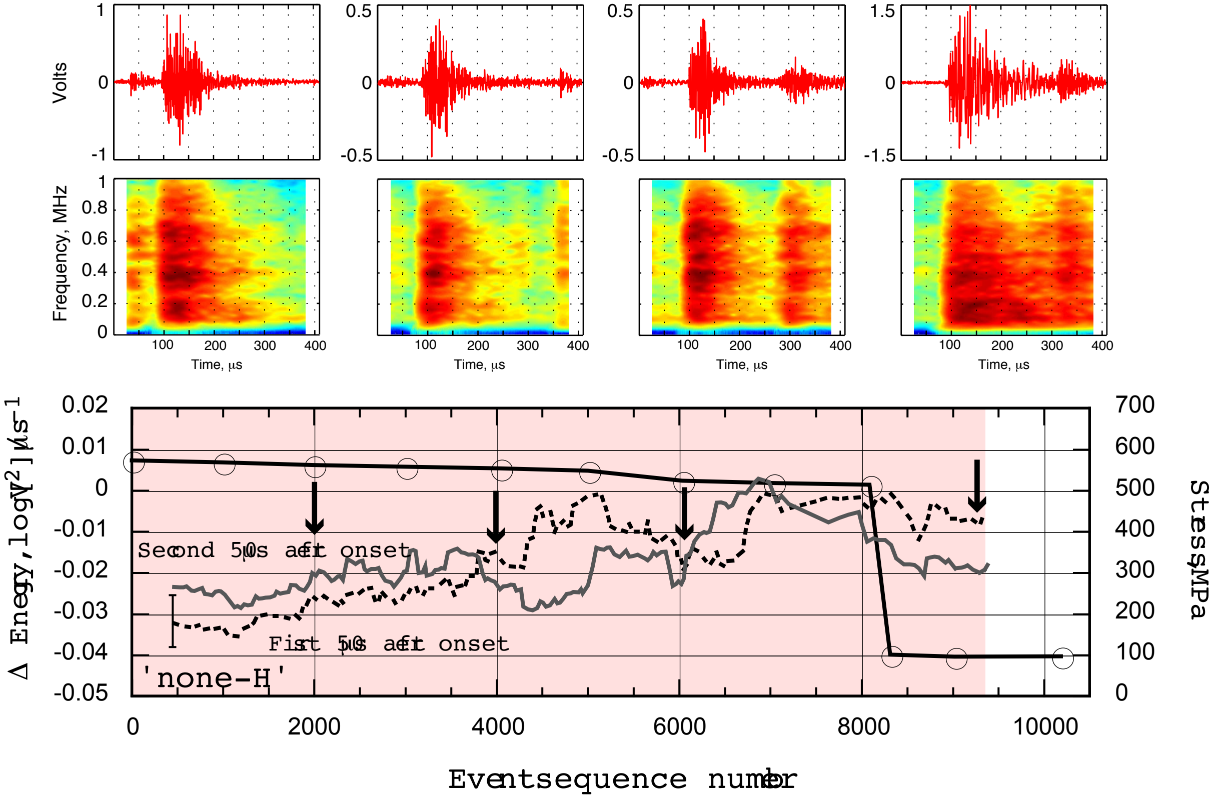

Volts
Frequency, MHz
Time, μs
Second 50 μs after onset
First 50 μs after onset
'none-H'
Δ Energy, log[V²] μs⁻¹
Stress, MPa
Event sequence number

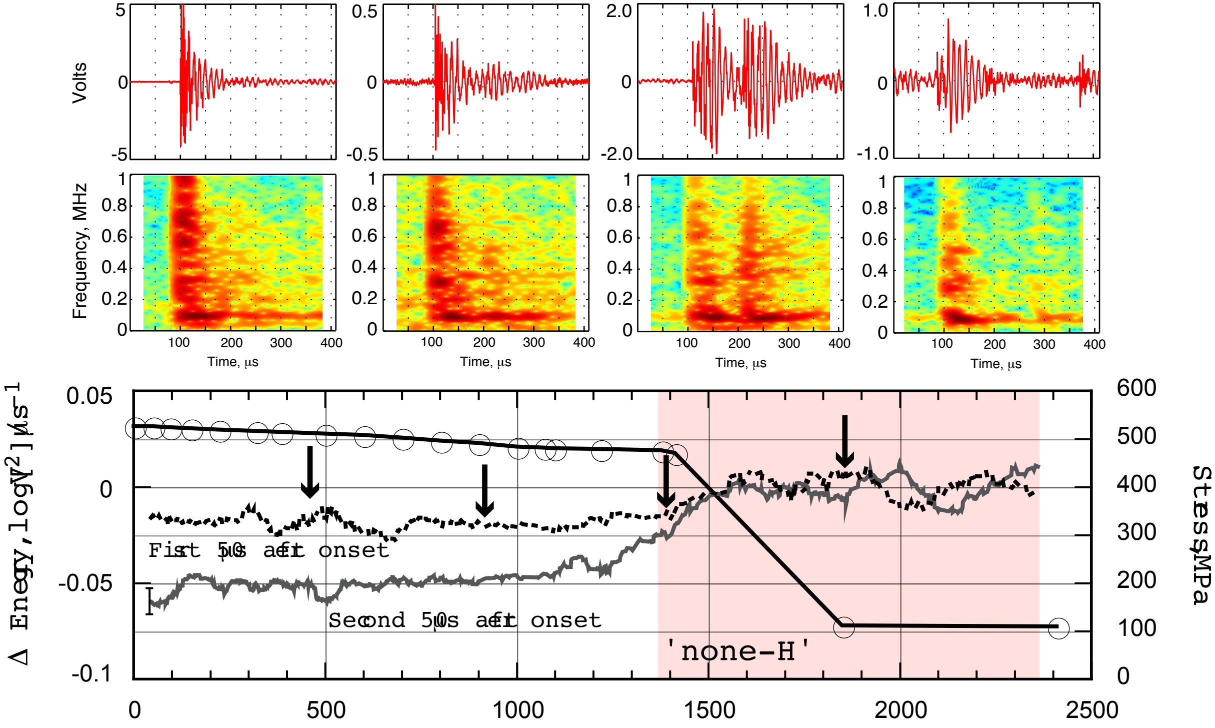

Volts
Frequency, MHz
Time, µs
First 50 µs after onset
Second 50 µs after onset
'none-H'
Δ Energy, log[V²] µs⁻¹
Stress, MPa